Simulation Study of the Structure and Dynamics of the Alzheimer's Amyloid Peptide Congener in Solution

Francesca Massi,* Jeff W. Peng,† Jonathan P. Lee,* and John E. Straub*
*Department of Chemistry, Boston University, Boston, Massachusetts 02215; and †Protein NMR Group, Vertex Pharmaceutical Inc., 130 Waverly Street, Cambridge, Massachusetts 02139 USA

ABSTRACT The amyloid Aβ(10–35)-NH_2 peptide is simulated in an aqueous environment on the nanosecond time scale. One focus of the study is on the validation of the computational model through a direct comparison of simulated statistical averages with experimental observations of the peptide's structure and dynamics. These measures include (1) nuclear magnetic resonance spectroscopy-derived amide bond order parameters and temperature-dependent H_α proton chemical shifts, (2) the peptide's radius of gyration and end-to-end distance, (3) the rates of peptide self-diffusion in water, and (4) the peptide's hydrodynamic radius as measured by quasielastic light scattering experiments. A second focus of the study is the identification of key intrapeptide interactions that stabilize the central structural motif of the peptide. Particular attention is paid to the structure and fluctuation of the central LVFFA hydrophobic cluster (17–21) region and the VGSN turn (24–27) region. There is a strong correlation between preservation of the structure of these elements and interactions between the cluster and turn regions in imposing structure on the peptide monomer. The specific role of these interactions in relation to proposed mechanisms of amyloidosis is discussed.

BACKGROUND

A persuasive argument has been made to support the hypothesis that amyloid peptide deposition is "a necessary but not sufficient factor for the pathogenesis" of Alzheimer's disease (Selkoe, 1991). From the analysis of experimental studies of amyloidogenesis, several distinct scenarios for fibril formation and elongation have evolved (Lansbury, 1996; Maggio and Mantyh, 1996; Teplow, 1998; Rochet and Lansbury, 2000). In one scenario, largely unstructured peptide monomers in solution cluster and form nuclei (Lansbury, 1996). When the cluster reaches a critical "nucleus," that nucleus then grows to form full length fibrils by the addition of monomers to the existing fibril ends (Lomakin et al., 1996, 1997). In a second scenario, there is first the formation of peptide "protofibrils" of intermediate length (Harper, 1997a; Walsh, 1997). Such protofibrils then associate to form full length fibrils (Walsh, 1997; Harper, 1997b). Once the full length fibrils are formed, additional amyloid peptide may add directly to existing fibrils (Esler, 1996a; Kusumoto, 1998). Finally, monomers may associate to form micelles. Those micelles may convert to fibril nuclei upon reaching a critical size (Lansbury, 1996; Lomakin et al., 1996, 1997). The relative importance of each of these possible pathways has not yet been established.

Once the fibrils are formed, it has been clearly demonstrated that the process of elongation of those existing fibrils occurs through the process of monomeric peptide binding to fiber ends (Esler, 1996a) and that the kinetics are first order in the concentration of monomeric peptide. This key observation has motivated studies of the simple first order kinetics of fibril elongation (Teplow, 1997; Kusumoto, 1998).

In such a mechanistic theory of fibril elongation an important question is raised. How does the peptide's solution phase structure influence the rate of fibril elongation? The wild-type (WT) peptide congener has been shown to exist in a loosely formed collapsed coil state in aqueous solution (Lee et al., 1995; Zhang et al., 1998). The structure of the collapsed coil is characterized by a central hydrophobic cluster (CHC) in the LVFFA (17–21) region. There is also a dominant turn in the VGSN (24–27) region that is observed in both the aqueous solution structure and the trifluoroethanol (TFE)-water solution structure, which shows two short α-helical regions (Barrow et al., 1992). This has been supported by H_α chemical shift measurements taken as a function of temperature (Zhang, 1999), which have shown very small changes in the chemical shift over a range of temperature from 5 to 35°C in the VGSN region. Analysis of the exposed hydrophobic surface area of the collapsed coil structure shows that the peptide presents a large hydrophobic patch that could play an important role in the initial deposition of the peptide monomer on the fibril surface.

Experimental analysis of the E22Q Dutch mutant of the amyloid peptide has shown it to be significantly more active than the WT peptide with a twofold increase in the rate of fibril elongation and deposition competence. Experimental measurement of the H_α proton chemical shift in the wild type and Dutch mutant indicates that the structures of the monomeric peptides in solution are similar (Esler et al., 2000). The increased deposition rate observed for the Dutch mutant has been explained in terms of a more disordered solution state relative to the WT peptide (Esler et al., 2000). The looser structure is believed to lower the entropic barrier

Received for publication 9 March 2000 and in final form 28 September 2000.

Address reprint requests to Dr. John E. Straub, Boston University, Department of Chemistry, 590 Commonwealth Ave., Boston, MA 02215. Tel.: 617-353-6816; Fax: 617-353-6466; E-mail: straub@bu.edu.

0006-3495/01/01/31/14 $2.00

for opening of the peptide, which is necessary in the deposition process.

Experimental studies of Aβ(10–35)-NH_2-cycloH14K-E22, an engineered cyclic peptide congener, has demonstrated that the covalently locked structure is similar to the structure of the WT peptide (Esler et al., 2000). However, the structurally locked cyclic congener is found to be inactive in deposition. This has been interpreted as a demonstration that the peptide must be allowed to adopt an extended conformation in order to add to an amyloid template.

Nuclear magnetic resonance spectroscopy (NMR) structural analysis of the F19T congener of the amyloid peptide congener in aqueous solution indicates that there is a serious disruption of peptide structure in the CHC region of the mutant peptide (Esler et al., 1996b). This disruption of the CHC is correlated with a diminished ability of the peptide to add to well-formed amyloid deposits. Therefore, in both the F19T congener and the E22Q Dutch mutant, the amyloid peptide monomer in solution is found to be less constrained in the coil state. In the case of the E22Q Dutch mutant and the WT peptide, the structure of the CHC is preserved and peptide activity is normal or increased. In the case of the cyclic congener, the CHC is preserved and the peptide initially adheres to the fibril. However, the restricted peptide cannot undergo the necessary conformational transition required to add to the fibril. In the case of the F19T congener, the CHC and hydrophobic patch are disrupted and activity is diminished (Esler et al., 1996b).

The scenario that emerges from these studies is one in which a partially structured collapsed coil state encounters the fibril end through diffusion and adheres to the fibril end to bury its hydrophobic patch. The peptide deposits itself on the fibril end, resulting in a loosely formed complex. The peptide/fibril complex then undergoes reorganization to accommodate the peptide in a more fully deposited (product) state. The reorganization step may involve conformational changes in the peptide and/or the fibril end. The activation energy for the fibril elongation is associated with peptide/fibril reorganization.

All of this evidence clearly points to a central role of the structure and dynamics of the peptide monomer in the mechanism of fibril elongation. There is evidence that the structure of the monomer in solution is intimately related to the process of monomer deposition and reorganization on the preexisting fibril surface. Therefore, knowledge of the structure of the monomer is essential in understanding the rate of diffusion of the monomer in solution.

In this study, we develop a model of the WT peptide congener in aqueous solution and use that model to simulate the peptide dynamics on a nanosecond time scale. Our focus is on validating our model by direct comparison with experimental studies and augmenting the existing body of experimentally derived information regarding the peptide's structure and dynamics. Specifically, we pose the following questions. (1) How well can simulation represent the computed NMR structural order parameters for the peptide in solution, the rate of peptide diffusion, and the observed hydrodynamic radius? (2) Are there structural motifs that characterize the conformations of the monomer in solution? (3) What interactions stabilize the monomer structure and what role do those interactions play in the peptide's "activity"?

To answer these questions, multiple trajectories were run originating from independent starting conformations of the peptide. From these trajectories, the peptide structure, intramolecular fluctuations, and overall peptide dynamics were analyzed. Direct comparison is made with a variety of experimental observables. The analysis points to specific, key interactions that stabilize the structure of the peptide monomer. The role of these interactions in the process of peptide deposition and fibril elongation is discussed.

METHODS

The WT peptide congener is depicted in Fig. 1. The structure was derived using NMR by Lee and coworkers (Zhang et al., 2000) from distance geometry calculations employing NMR-derived NOE restraints. The colored regions are Tyr10-Glu11-Val12 (purple), His13-His14 (gray), Gln15-Lys16 (purple), Leu17-Val18-Phe19-Phe20-Ala21 (red), Glu22 (green), Asp23 (pink), Val24-Gly25-Ser26-Asn27 (yellow), Lys28-Gly29-Ala30-Ile31-Ile32-Gly33-Leu34-Met35 (purple). Of primary interest in this work is the 17–21 LVFFA segment (red) that forms the central hydrophobic cluster and the 24–27 VGSN (yellow) segment that forms a stable turn.

Our simulations each originated from one of a set of four initial peptide structures that were chosen from two families of C-terminus conformers. Those structures resulted from a distance geometry refinement combined with a molecular dynamics annealing/minimization procedure employing experimentally derived NOE restraints. NMR heteronuclear relaxation data was also used to successfully compute S^2 order parameters for a number of the backbone amide H-N vectors. Further fitting of the relaxation data together with estimation of the shape factors and hydrodynamic radii from NMR based translational diffusion measurements allowed for two inde-

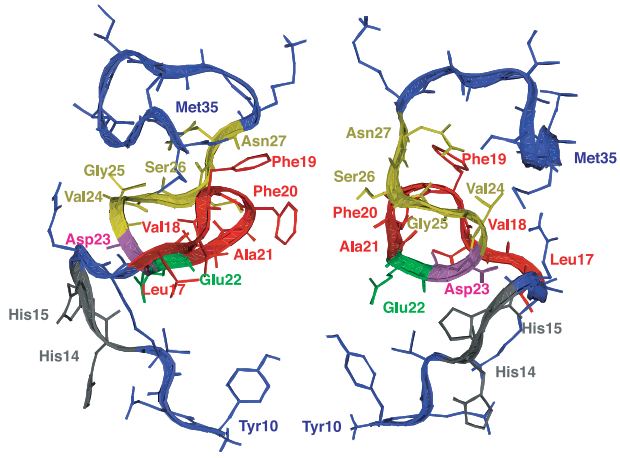

FIGURE 1 This master figure identifies the important groups of residues that compose the wild-type congener amyloid β(10–35)-NH_2 peptide. From the N-terminus the groups are Tyr10-Glu11-Val12 (blue), His13-His14 (gray), Gln15-Lys16 (blue), Leu17-Val18-Phe19-Phe20-Ala21 (red), Glu22 (green), Asp23 (purple), Val24-Gly25-Ser26-Asn27(yellow), Lys28-Gly29-Ala30-Ile31-Ile32-Gly33-Leu34-Met35 (blue).

pendent estimates of the rotational correlation time which were in good agreement. For completeness, in this section we provide a brief description of the experimental approach used to determine the set of initial structures, order parameters and peptide diffusion constants employed in our study. Further details may be found elsewhere (Lee et al., 1995; Zhang, 1999; Zhang et al., 2000).

In the remainder of this section we describe the simulation model employed in our study. The standard methods used to determine the peptide's structure, NMR order parameters, time dependent structural changes, and rates of self-diffusion are briefly summarized.

Experimental methods

NMR sample preparation

A Merrifield solid phase synthesis was used to build the Aβ(10–35)-NH_2 peptide that was subsequently purified to greater than 98% homogeneity by HPLC. A first sample was uniformly labeled with ^{2}H at Val12, Leu17, Val18, Phe19, Ile32, and Leu34, ^{15}N in the backbone position of Phe19, Val24, Gly25, and Gly29, and ^{13}C uniformly at Val24, in the β-methyl groups of Ala21 and Ala30 and the ϵ-methyl group of Met35. A second sample was uniformly labeled with ^{2}H at Val12, Leu17, Phe19, Val24, Ile31, and Leu34, ^{15}N in the backbone position of Val18, Phe20, Gly25, and Gly29, and Gly33, and ^{13}C uniformly at Val24, in the β-methyl groups of Ala21 and Ala30 and the β-methyl group of Met35. The use of ^{15}N- and ^{13}C-labeled samples resulted in the unambiguous identification of a larger number of ^{1}H-^{1}H NOEs, thereby increasing the number of restraints that could be subsequently employed in the structural refinement. The use of extensive ^{2}H labeling of Leu, Val and Ile residues aided in the identification of cross peaks in the Leu, Val, Ile CH_3 fingerprint region. This effort was only partially successful in resolving the methyl resonances of Ile31, Ile32, and Leu34. The ^{2}H labeling of the Phe19 and Phe20 residues aided in the unique assignment of these key residues of the central hydrophobic core in the crowded aromatic region.

Dried samples were used to make an approximately 250 μM concentration of peptide in either 100% D_2O or a 90:10 ratio of H_2O:D_2O with 0.5 mM sodium 3-(trimethylsilyl)propionate-2,2,3,3,-d_4 (TSP) where the pH was adjusted to approximately 5.6 using hydrochloric acid or ammonium hydroxide (deuterated when appropriate). The resulting solutions were immediately centrifuged for 10 min at 100,000 $\times$ g and then, the centrifugation was continued to achieve a sedimentation of particles greater than 0.5 s. That criterion would demand, depending on the centrifuge, ultracentrifugation for 100 to 200 hours. The intensive centrifugation is an essential step in the preparation of the samples of predominately monomeric peptide required for structural analysis. Intensive centrifugation has been shown to lead to samples 200–300 μM in peptide that are stable and show no signs of aggregation for periods in excess of 3 years.

NMR experiments

Data for ^{1}H spectra were collected for samples maintained at 10°C on 11.7 T (located at Boston University) and 17.6 T (located at Oxford Instruments, Oxford, UK) Varian UNITYplus NMR machines employing pulse field gradient probes. The design of the structural work, presented in detail elsewhere (Lee et al., 1995; Zhang et al., 2000), is the following. The chemical shifts, referenced to internal TSP at 0.00 ppm, were detected using two-dimensional waveform gradient suppression total correlation spectroscopy (TOCSY) with frequency discrimination achieved through the time-proportional phase-incrementation (TPPI-States) method. ^{1}H detected heteronuclear multiple quantum coherence nuclear Overhauser enhancement spectroscopy (NOESY) spectra were taken to determine the isotope filtered ^{15}N edited spectra.

Structural refinements using NOE restraints

Structures of the peptide that were consistent with the experimentally derived NOE restraints were computed using the Distance Geometry II module of the Insight II computational software package (Molecular Simulations, San Diego, CA). There were 55 inter-residue and 24 intra-residue NOEs observed for the peptide's N-terminal (Tyr10-Lys16) region; 86 inter-residue and 31 intra-residue NOEs were detected for the central hydrophobic cluster (Leu17-Ala21); 46 inter-residue and 22 intra-residue NOEs were measured for the extended core (Glu22-Lys28); for the C-terminal peptide region (Gly29-Met35) 28 inter-residue and 24 intra-residue NOEs were observed. The measured NOEs resulted in the total of 84 sequential, 66 medium range (i,i + 2 or i,i + 3), and 32 long-range restraints used in the distance geometry calculations.

A set of 40 peptide structures resulted from the distance geometry calculations. A subset of those structures was then used as input in a series of molecular dynamics (MD) calculations performed using the DISCOVER program of the Insight II computational software program. The MD calculations employed loose harmonic restraints of atoms about their initial positions and consisted of 1 ps of dynamics at 1000 K followed by a stepwise cooling to 200 K at a rate of 100 K/ps. The energy of the final "annealed" structure was then minimized using the conjugate gradient algorithm. Of the starting set of 40 peptide structures, following the MD annealing and minimization procedure, 15 structures with the lowest potential energy (in the absence of solvent) were selected to represent the solution state ensemble of monomeric peptide. The 15 final structures can be grouped in two main structural families depending upon the orientation of the C-terminus. The root mean square deviation (RMSD) of the backbone atoms (N-C_α-C) has been calculated for both families separately. It showed consistently smaller values for one of the two families in every region of the peptide. The RMSD in the region of the central hydrophobic cluster and extended core (Lys 16-Lys28) was 0.47 Å and 0.58 Å respectively for the two families of structures. This result is different from the one reported by Lee (Zhang et al., 2000), since a different definition of the RMSD has been used (Molecular Simulations). Outside of the peptide's core region, the C-terminal residues (Gly29-Met35) were relatively well-structured in one of the two families with a backbone RMSD of 0.57 Å, and less well structured in the other with an RMSD of 1.00 Å. However, the N-terminal region was significantly less structured in solution resulting in an absence of medium- and long-range NOE restraints with RMSD values of 1.01 and 1.20 Å. The four initial structures employed in our MD simulations were taken to be the two lowest-energy structures from each family.

Diffusion

Diffusion constants for the peptide were measured as described elsewhere (Tseng et al., 1999). Briefly, the pulse field gradient probe was used to tailor a trapezoidal spatial gradient, the amplitude of which could then be arrayed. The NMR gradient amplitude dependence of the signal intensity was then measured and fitted to an exponential function of the squared gradient amplitude. The decay rate of the exponential was assumed to be proportional to the peptide diffusion constant. Ten values of the gradient amplitude were used in each of three complete measurements.

Measurement of ^{15}N relaxation times

One approach to the determination of the amide bond vector order parameters, S^2 is known as spectral density mapping (Peng and Wagner, 1992, 1995). In that approach, a series of rates for (1) longitudinal ^{15}N magnetization relaxation, $R_N(N_z)$; (2) in-phase ^{15}N single quantum coherence relaxation, $R_N(N_x)$; (3) antiphase ^{15}N single quantum coherence relaxation, $R_{HN}(2H_z^N\ N_x)$; (4) longitudinal heteronuclear two-spin order relaxation, $R_H(2H_z^N\ N_z)$; (5) amide proton longitudinal relaxation, $R_H(H_z^N)$; and (6) longitudinal cross-relaxation between the amide proton and nitrogen,

$R_N(H_z^N \leftrightarrow N_z)$, were measured. A set of constraint equations relaters the set of relaxation rates to the spectral density $J(\omega)$ at five frequencies 0, ω_H, ω_N, and $|\omega_H| \pm |\omega_N|$, and the sum of the proton longitudinal relaxation rate constants. The spectral density may then be fit using a model free approach to derive the S^2 order parameters (Cavanagh et al., 1996).

In this work, the reduced spectral density mapping protocol was followed (Peng and Wagner, 1995). It is assumed that at high magnetic fields $J(\omega_H) \approx J(\omega_N + \omega_H) \approx J(\omega_H - \omega_N)$, i.e., the differences are less than the typical error in measuring relaxation rates. This assumption eliminates two of the six (relaxation) equations, reducing the set of equations to four. However, the sum of the proton longitudinal relaxation rate constants is, under this assumption, decoupled, thereby resulting in three equations relating three values of the spectral density $J(0)$, $J(\omega_N)$, and $J(\omega_H)$ to $R_N(N_z)$, $R_N(N_x)$, and $R_N(H_z^N \leftrightarrow N_z)$ or equivalently T_1, T_2, and the NOE where the steady-state heteronuclear NOE, η, is defined (Peng and Wagner, 1992):

$$\eta = \frac{\gamma_H}{\gamma_N} \frac{R_N(H_z^N \leftrightarrow N_z)}{R_N(N_z)}. \quad (1)$$

The relaxation rates measured at B_0 field strength of 11.74 T were then used to solve for the spectral density at the three specified frequencies. The spectral density was, in turn, fitted using the Lipari-Szabo model free formalism, which incorporates overall molecular reorientation with a time constant τ_c (the mean time required for the molecule to rotate by one radian) and intramolecular or "internal" motions with a time constant τ_{int} (Lipari and Szabo, 1982a,b). By fitting the spectral density to the prescribed functional form, it was possible to derive the squared generalized order parameters, S^2, for the individual amide bond vectors. In that procedure, $J(0)$ was ignored and $J(\omega_N)$ and $J(\omega_H)$ were fit to determine values of S^2 and τ_{int} using a value of $\tau_c = 1.3$ ns/rad. Those parameters were then used to predict $J(0)$. The experimentally derived values of $J(0)$ were somewhat higher than the back-predicted values, suggesting the presence of conformational exchange. The back-predicted values are nonetheless in reasonable agreement with the experimental values. This suggests that the resulting values of S^2 are reliable.

Simulation model of the WT peptide congener in aqueous solution

The NMR structure of the amyloid β-peptide served as the starting configuration of the simulation. The peptide was centered in a rhombic dodecahedron cell that was carved from a cubic box of 50 Å on a side and filled with 2113 water molecules (for a 31 mM concentration of peptide). Periodic boundary conditions were applied to avoid edge effects. The energetics of the Aβ peptide in water was simulated using the version 22 potential energy function of the CHARMM program (Mackerell et al., 1998). The potential energy cutoff distance for the nonbonding interactions was 12.0 Å. Ewald summation was used to evaluate the electrostatic interactions. The use of the SHAKE constraint algorithm throughout the simulation, to keep the lengths of the bonds involving hydrogen atoms fixed at their equilibrium values, allowed for the use of a time step of integration of 2 fs using the CHARMM program (Brooks et al., 1983). After the equilibration period of 200 ps, a production run of 1 ns was completed with an average temperature of 300K. Coordinates and energetic data were collected every 200 fs.

The starting configurations for our peptide simulations were taken from a set of coordinates derived from distance geometry calculations and modeling with NMR derived NOE restraints. The four structures are depicted as ribbons in Fig. 2. The four 1-ns trajectories are denoted T1, T2, T3, and T4. What is in common to the four structures is the conformation of the 17–27 region containing the LVFFA and VGSN substructures. Outside of that core structure there is considerable disorder. In those regions, the experimentally derived restraints are fewer, but nonetheless consistent with some residual structure.

FIGURE 2 The four initial configurations of the peptide superimposed to best overlap the 17–21 LVFFA regions of the peptides. Each initial structure was generated through a refinement procedure using NOE restraints derived from NMR experiments on the wild-type congener amyloid β(10–35)-NH_2 peptide by Lee and coworkers. Note the significant disorder outside of the central core region.

Measures of peptide dynamics and reorganization

We employ a number of useful measures of the peptide dynamics, including the rate of translational diffusion of the peptide and variations in the compactness of the peptide as measured by the radius of gyration and peptide end-to-end distance. Comparisons are made with the theoretical estimates for a freely jointed linear chain.

Self-diffusion constant for the peptide

The mean-square displacement of the center-of-mass of the peptide was computed as a function of time for the trajectories T1, T2, T3, and T4. The diffusion constant of the peptide monomer was estimated using the Einstein relation

$$\langle \Delta r_{COM}(t)^2 \rangle \sim 6Dt \quad (2)$$

which is expected to hold in the limit of long times. The mean square displacement was computed over the length of the trajectory and the slope was measured to determine the diffusion constant.

The magnitude of the diffusion constant was also estimated using the Kubo relation,

$$D = \frac{1}{3} \int_0^\infty \langle \mathbf{v}_{COM}(t) \mathbf{v}_{COM}(0) \rangle dt \quad (3)$$

where $\langle \mathbf{v}_{COM}(t) \mathbf{v}_{COM}(0) \rangle$ is the velocity autocorrelation function for the center-of-mass of the peptide. The velocity autocorrelation function was computed and fitted to an exponential function to estimate the time integral and D.

Peptide end-to-end distance

The end-to-end distance of the peptide was defined by the distance separating the first N atom of the N-terminus of Tyr10 and the second end N atom attached to the carbonyl oxygen of the C-terminal residue Met35. This is equivalent to a sum along the backbone according to

$$r_e = \left| \sum_i l_i \right| \quad (4)$$

where l_i is the vector connecting the consecutive N atoms along the back-bone between the N- and C-termini. This distance was computed for each simulation. We write the ensemble-averaged value $\langle r_e^2 \rangle$, which is computed by averaging over the MD trajectories. Large changes indicate significant reorganization in the global structure of the peptide.

Radius of gyration

The radius of gyration for the peptide was computed using all of the peptide atoms in the standard formula (Berne and Pecora, 1976)

$$r_g^2 = \sum_k^N m_k (r_k - r_{COM})^2 \Big/ \sum_k^N m_k \tag{5}$$

where r_{COM} is the peptide's center of mass, r_k is the position of the kth atom in the peptide, and m_k is its mass. When the masses are all equal, this expression is equivalent to a sum over all atom pair distances r_{ij} as

$$r_g^2 = \frac{1}{N^2} \sum_{i<j} r_{ij}^2 \tag{6}$$

In our computations, r_g was computed using (1) all atoms and (2) only the heavy (non-hydrogen) atoms. Each computation was carried out over many configurations of the peptide generated over the trajectory to determine the ensemble-averaged value $\langle r_g^2 \rangle$.

Characterizing the peptide structure in solution

Direct visualization of the peptide structure's time evolution was used as part of the analysis of the peptide dynamics. In addition, we analyzed the intramolecular hydrogen bond network by computing a measure of persistence for all possible hydrogen bonds. We also analyzed the evolution of the peptide structure by computing the solvent exposed surface area of the total peptide and the hydrophobic patch centered about the LVFFA region. These methods are defined below.

Recognizing intramolecular hydrogen bonds

In each stored configuration, the peptide was analyzed for hydrogen bonding groups for all possible donors and acceptors. The hydrogen bonding frequency was then computed for the full simulation by dividing the number of snapshots showing hydrogen bonds by the total number of snapshots. The approximate definition of the hydrogen bond that was used is that the donor and acceptor atoms must be at a distance shorter than or equal to 2.5 Å and the angle between the donor and acceptor diatomic groups is in the range 113–180° (Simmerling et al., 1995).

Solvent exposed surface area of the LVFFA region

The atomic exposed surface area was computed by the method described by Wesson and Eisenberg (1992) and originally developed by Lee and Richards (1971). Essentially, the solvent exposed surface area of each atom was defined as the area exposed to contact by a water probe of diameter 2.8 Å. The total surface area for the peptide in a modeled extended configuration was computed to represent an upper bound on the surface area of the peptide. Each trajectory was then analyzed by computing the total solvent exposed surface area of the whole peptide molecule and the atoms composing the LVFFA region.

Characterizing internal motions: Lipari-Szabo NMR order parameters

We follow the standard "model free" analysis of Lipari and Szabo (1982a,b). The motion of the peptide can be described by a correlation function $C(t)$ for the orientation of a peptide backbone amide bond vector. Assuming that the internal motions are uncorrelated with the overall molecular tumbling, $C(t)$ can be separated into two contributions: one for the internal motions, $C_{int}(t)$, and the other for the overall molecular rotation, $C_{tumb}(t)$.

$$C(t) = C_{tumb}(t) C_{int}(t) = \frac{1}{5} e^{-t/\tau_0} C_{int}(t) . \tag{7}$$

$C_{int}(t)$ is given by

$$C_{int}(t) = \frac{4\pi}{5} \langle r^{-6} \rangle^{-1} \sum_{m=-2}^{2} \left\langle \frac{Y_{2m}(\theta(t),\phi(t)) Y_{2m}^*(\theta(0),\phi(0))}{r(t)^3 r(0)^3} \right\rangle \tag{8}$$

where $Y_{2m}(\theta, \phi)$ are the second order spherical harmonics and θ and ϕ are the spherical polar angles that specify the orientation of the internuclear NH amide bond vector in the molecule-fixed coordinate frame.

The internal motions of the peptide can be characterized by the two parameters S^2, a generalized order parameter, and τ_{int}, an effective correlation time, defined through

$$S^2 = \lim_{t\to\infty} C_{int}(t) = \frac{4\pi}{5} \langle r^{-6} \rangle^{-1} \sum_{m=-2}^{2} \left| \left\langle \frac{Y_{2m}(\theta,\phi)}{r^3} \right\rangle \right|^2 \tag{9}$$

and

$$\tau_{int} = \frac{1}{C_{int}(0) - S^2} \int_0^T (C_{int}(t) - S^2) dt \tag{10}$$

where T is the time after which $C_{int}(t) = S^2$. $C_{int}(0)$ is the value of the internal correlation function at time zero.

S^2 is a measure of the degree of freedom of the motion of the intermolecular amide bond vector; S^2 is equal to 1 if the motion is completely restricted and is equal to 0 for isotropic motion. In order to separate the overall molecular rotation from the internal motion, every coordinate frame of the 1 ns trajectory was translated and rotated until the root mean square displacement with respect to a reference configuration ($t = 0$) was minimized (Philippopoulos and Lim, 1994).

RESULTS

This section summarizes the analysis of the four nanosecond trajectories of the solvated Aβ-peptide congener dynamics. The peptide dynamics is described and connection with experiment is made through the computation of NMR order parameters and rates of peptide self-diffusion and reorganization.

Peptide structure in solution

The structural dynamics of the peptide is depicted for the four trajectories in Fig. 3. In each "movie" the peptide is

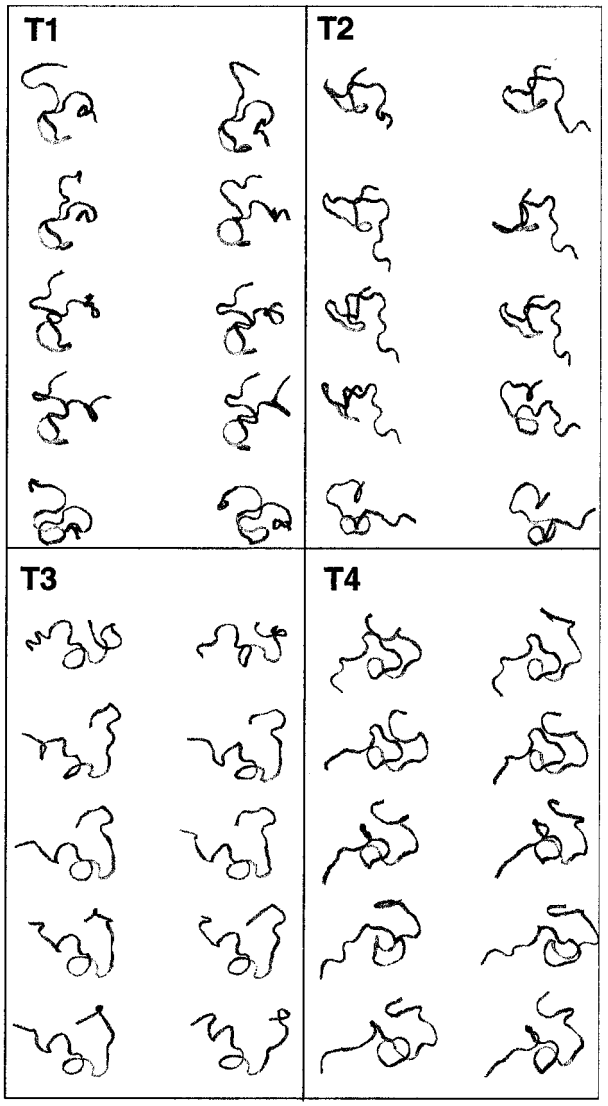

FIGURE 3 A "movie" composed of snapshot configurations taken every 100ps along the nanosecond trajectories T1, T2, T3, and T4, respectively.

rendered every 100 ps during the nanosecond duration of the run. In trajectories T1, T2, and T4 the core of the peptide structure is seen to be maintained. The N- and C-terminal peptide regions are less well structured.

The character of the global peptide fluctuation is even more apparent in Fig. 4, in which the snapshots of the peptide depicted in Fig. 3 are reoriented so as to best fit the LVFFA (17–21) region for all structures. A striking feature is the strong structural integrity of the central core of the peptide, in particular the LVFFA (17–21) region and the VGSN (24–27) turn region. This is the case in all trajectories. A slight difference in simulation T3 is that the core of the structure is disrupted and the end-to-end distance in the peptide is significantly decreased over the simulation run. This transition will be discussed in detail below.

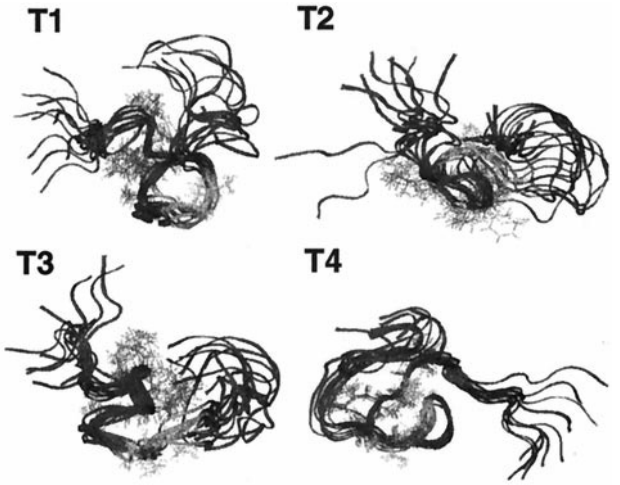

FIGURE 4 A "collage" composed of snapshot configurations taken every 100ps along the nanosecond trajectories T1, T2, T3, and T4, respectively. The peptide backbone structures are overlapped to best fit the 17–21 LVFFA regions of the peptide.

Hydrogen bond formation

A plot of the hydrogen bond frequency, computed as the fraction of time a hydrogen bond is well-formed during the trajectory, is shown in Fig. 5. In simulation T1, the hydrogen bonds that are most persistent include Glu11(O)-His13(HN), seen in all four runs, Val18(O)-Lys28(HN), Ser26(hydroxylic H)-Asn27(HN), and Lys16(O)-Val18(HN). Other hydrogen bonds that are formed in this trajectory include Leu17(O)-Phe19(HN), Ala21(O)-Asp23(HN), and Lys28(O)-Val18(HN). We find that for this run, amino acids in the VGSN turn region do not form hydrogen bonds with the LVFFA region. During this run, the only hydrogen bonds to form in either region are those internal to the region.

In simulation T2 we find Asn27 (side chain acyl oxygen)-Ala30(HN), Glu11(O)-His13(HN), and Ile32(O)-Asn27 (sidechain HN) to be persistent hydrogen bonds. In addition to those hydrogen bonds, also seen in the T2 run are hydrogen bonds between Phe20(O)-Ser26(hydroxylic H), Ala21(O)-Gly25(HN), Leu17(O)-Phe19(HN), and Ala21(O)-Asp23(HN), all of which involve at least one atom of the LVFFA region. Two of these bonds are between the LVFFA and the VGSN regions. The last two bonds listed above are also present in the T1 run. In simulations T2 and T4, there is a hydrogen bond between Asp23(O)-Gln15(HN).

In simulation T3, the peptide structure appears to be more open. Persistent hydrogen bonds are formed between Ser26(hydroxylic O)-Asn27(HN), His14(O)-Val18(HN), and His13(O)-Gln15(HN). The backbone oxygen of the Phe19 residue interacts with both Gly25(HN) and Val24(HN). Those interactions involve residues from the LVFFA and VGSN regions. A hydrogen bond between Ala30(O)-Ile32(HN) is also seen. Hydrogen bonds involv-

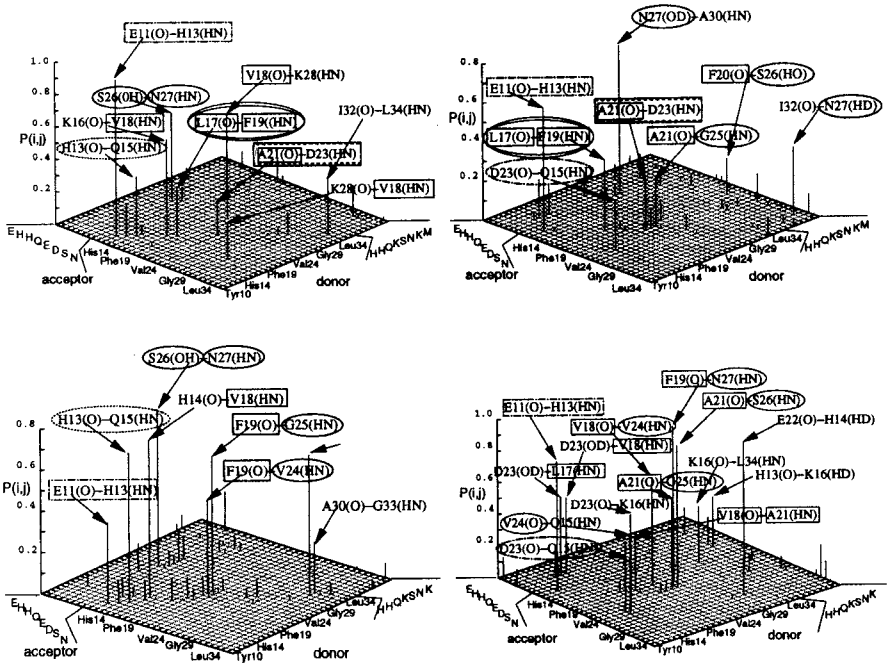

FIGURE 5 Plot of the hydrogen bonding probabilities for simulations T1, T2, T3, and T4, respectively. Hydrogen bond acceptors are noted along the x-axis and donors are indicated along the y-axis. The acceptors indicated with single letters are side chain groups; those that follow are backbone carbonyl oxygen atoms. Similarly, the donors indicated with single letters are side chain groups; the remaining donors are backbone amide hydrogen atoms. On all four plots, different styles of boxes have been used to identify atoms from different regions on the peptide: rectangular solid line boxes for the LVFFA and oval solid line boxes for the VGSN region. Hydrogen bonds common to at least two different trajectories are indicated with an additional box, whose shape and line type are common among the trajectories.

ing Ala21 and Leu17 occur infrequently. This run presents the smallest number of common hydrogen bonds of all the trajectories.

In the T4 simulation, there is a high degree of structure. The H-bonds involve many residues; with the exception of Phe20, all of the amino acids between His13 and Asp27 are involved in hydrogen bonds within the region. The residues of the LVFFA region form many hydrogen bonds in the T4 run and many of those hydrogen bonds are formed with atoms in the VGSN region. Examples of such hydrogen bonds include Asp23 (side chain O)-Val18(HN), Asp23 (side chain O)-Leu17(HN), Phe19(O)-Asn27(HN), Val18(O)-Ala21(HN), Val18(O)-Val24(HN), Ala21(O)-Ser26(HN), and Ala21(O)-Gly25(HN). The backbone oxygen atom of the Asp23 residue also interacts with the backbone amide hydrogens of Gln15 and Lys16. Hydrogen bonds between Val24(O)-Gln25(HN), His13(O)-Lys16 (sidechain HN) and Glu22(O)-His14 (sidechain HN) are also seen. These extensive hydrogen bond networks are important to the stabilization of the core peptide structure.

Solvent-exposed surface area

The exposed hydrophobic surface area is thought to be crucial to the peptide's ability to recognize and adhere to the fibril end. The solvent-exposed surface area of the peptide is depicted in Fig. 6 for both the total peptide and the LVFFA central hydrophobic cluster region. Averaging over fluctuations, the LVFFA hydrophobic patch is approximately 400 $Å^2$ in extent, compared with the surface area of approximately 2600 $Å^2$ of the peptide as a whole.

There is a relatively high contribution of hydrophobic residues to the solvent-exposed surface area of the peptide in solution. It is interesting to notice that the nonpolar surface area is not evenly distributed on the peptide molecule, but is localized in a continuous patch on about one-third of the surface (Zhang et al., 2000).

In the T3 and T4 simulations, as the total solvent-exposed surface area of the peptide increases, the radius of gyration also increases. Note also that the T4 simulation shows the smallest values for the solvent-exposed surface area. That simulated structure is also the most rigid with small root-mean-square (RMS) atomic fluctuations and S^2 values.

Measures of peptide dynamics and reorganization

The most commonly used measure of the fluctuation in a peptide structure during a dynamic simulation is the RMS deviation in the position of each atom from its average value computed over the full simulation run. Those RMS deviations are plotted in Fig. 7 for the four runs. The magnitude of the RMS fluctuations provides the general description of the large scale motion of the N- and C-terminal regions. Large fluctuations also occur in the loop region centered about residue Glu22. The overall fluctuations in T4 are significantly lower than in the other three runs. In fact, the fluctuations in T4 are on the order of 1 Å, similar in magnitude to fluctuations observed in simulations of larger, globular proteins. Fluctuations in runs T1, T2, and T3 are significantly larger, on the order of 2 Å. In the T3 simula-

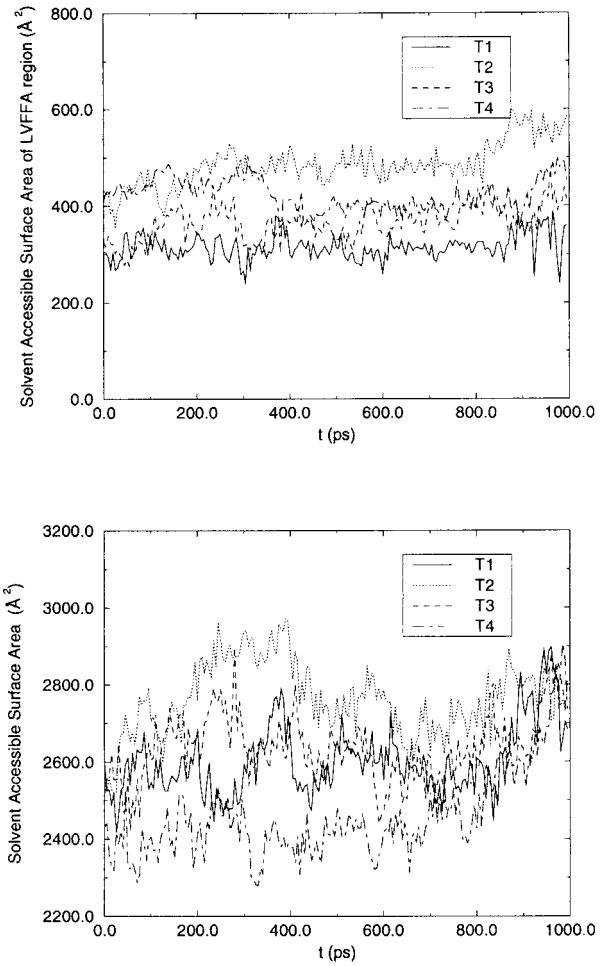

FIGURE 6 The atomic solvent exposed surface area contributed by the central hydrophobic cluster LVFFA (*top*) and the total peptide (*bottom*) over the length of the four simulation runs.

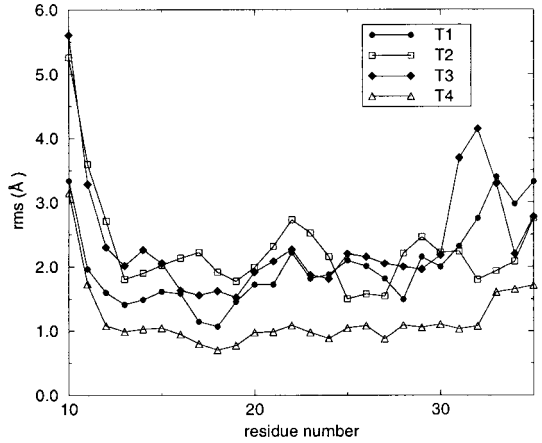

FIGURE 7 The averaged root-mean-square atomic coordinate deviation from the average peptide structure computed over the each of the four simulation runs.

tion there are very small values of S^2 for Ala21 and for residues 26–35. This is in agreement with the large RMS values for those regions.

Various NMR studies such as the proton chemical shifts show these regions to be particularly well structured in aqueous solution and reasonably insensitive to changes in temperature in the 5–35°C range (Zhang, 1999; see Fig. 8). In general, it can be seen that regions of small differential chemical shift correspond to regions of small RMS fluctuations. The overall picture is one of the peptide as a collapsed coil with significant structure imposed by the stable structure of the CHC LVFFA (17–21) and VGSN (24–27) turn regions and stabilized by their interactions (Zhang et al., 1998).

Peptide self-diffusion

The translational self-diffusion constant for the amyloid peptide was computed using the Einstein relation for the mean-square displacement of the peptide's center of mass. The results are depicted in Fig. 9, which shows the fits to the initial linear regions of the mean-square displacement and the resulting estimates of the diffusion constant. The average diffusion constant is approximately $D = 1.4 \times 10^{-6}$ cm^2/s.

The magnitude of the diffusion constant was also estimated by integrating over the velocity autocorrelation function depicted in Fig. 10. For the cases of trajectories T1, T3, and T4, the initial decay up to 2.0 ps is well approximated

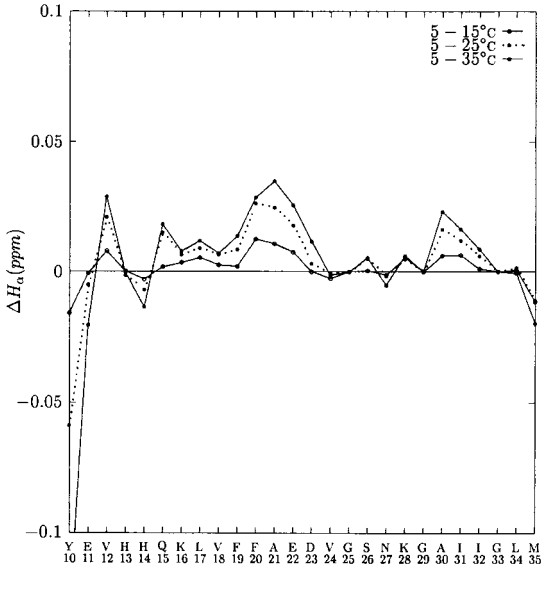

FIGURE 8 The difference between the values of the experimentally measured H_α proton chemical shift at temperature T and at temperature $T = 5°C$ ($\Delta H = H_\alpha(T) - H(5°C)$) as a function of the temperature over a range of 5 to 35°C. Small values indicate regions of the peptide where the average structure is stable over the measured temperature range (Zhang, 1999).

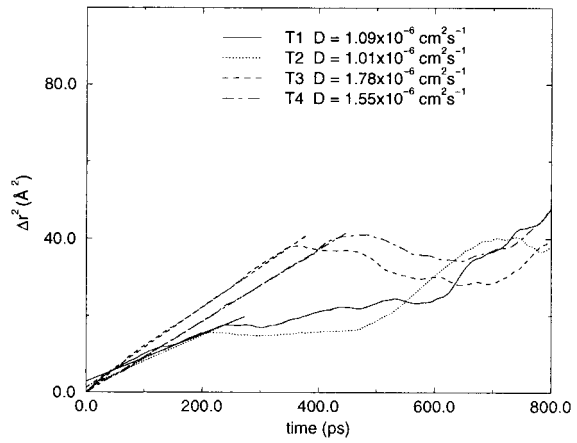

FIGURE 9 The mean square atomic displacement as a function of time for each of the four trajectories T1, T2, T3, and T4. The slope of the mean square displacement is equal to $6D$ where D is the self-diffusion constant. From this data were derived four estimates of the diffusion constant of the peptide.

by an exponential function of the form $C(t) = \langle v^2 \rangle \exp(-t/\tau)$ where the mean square velocity $\langle v^2 \rangle = 0.235$ Å^2/ps^2 = 2,350 m^2/s^2 for a root mean square velocity of 47 m/s as expected from kinetic theory for a peptide of mass $M = 2902$ g/mol. Using a simple fit to the exponential model where $\tau = 0.27$ ps, the estimate for the diffusion constant is $D = 2.1 \times 10^{-6}$ cm^2/s. This value is slightly larger than, but in reasonable agreement with, D values derived from fits to the mean-square displacement data. The experimentally measured value of the diffusion constant for the peptide in aqueous solution at this temperature is $D_{exp} = 1.4 \times 10^{-6}$ cm^2/s (Tseng et al., 1999). (A previous estimate of the diffusion constant was 1.6×10^{-7} cm^2/s, Kusumoto et al., 1998)

Suppose that we interpret the magnitude of the diffusion constant using a Langevin model. What is the value of the friction constant, γ, that results? Taking

$$D = k_B T/\gamma \tag{11}$$

we find that $\gamma = 1.9 \times 10^{-11}$ kg/s. Now suppose that we use the Stokes-Einstein relation

$$\gamma = 6\pi\eta r_H \tag{12}$$

where $\eta = 0.01$ poise is the viscosity of the water solvent. We estimate that the hydrodynamic radius of the peptide is $r_H = 10$ Å, which is in reasonable agreement with the estimates of the peptide radius computed over our simulated dynamics discussed in the following section.

In Fig. 11 we plot the dependence of the logarithm of the diffusion constant for a number of molecules (glycine, sucrose, ribonuclease, lysozyme, bovine serum albumin, and hemoglobin) along with the computed value for the Aβ peptide as a function of the logarithm of the molecular mass. Two fits are shown. The first fit is based on an approximation that the hydrodynamic radius a_H scales as $M^{1/3}$ where M is the mass of the molecule. The result is

$$D = 3.0 \times 10^{-5} \frac{1}{M^{1/3}} \text{ cm}^2/\text{s}\,. \tag{13}$$

This fit should work well if the molecule is closely packed. However, as we have seen, the peptide structure is somewhat extended in solution. A better fit to the mass scaling of the diffusion constant is achieved with

$$D = 5.1 \times 10^{-5} \frac{1}{M^{2/5}} \text{ cm}^2/\text{s} \tag{14}$$

although the mass scaling is less well founded. If the peptide was a linear chain we might expect r_H to scale as the peptide

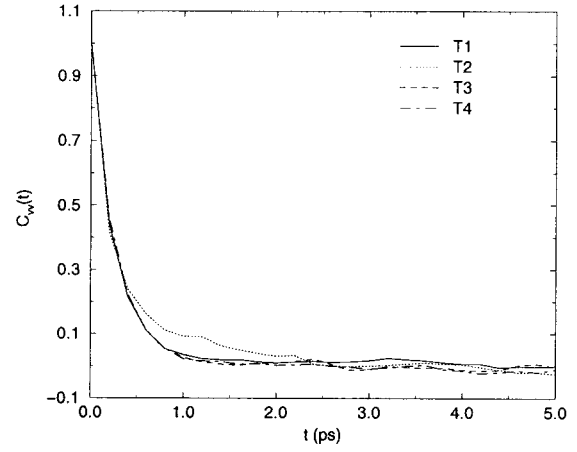

FIGURE 10 The velocity autocorrelation function for the center of mass motion of the peptide as a function of time for each of the four trajectories T1, T2, T3, and T4. For trajectories T1, T3, and T4, the decay is well approximated by an exponential function.

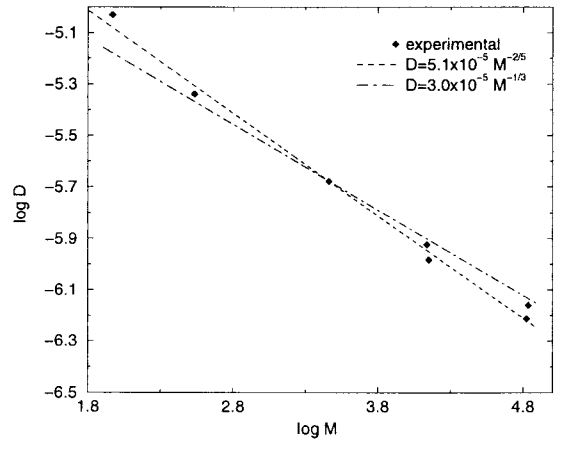

FIGURE 11 The log-log plot of the diffusion constant as a function of the molecular mass for a series of macromolecules (from experiment) and the β-amyloid peptide congener (from this work).

radius of gyration which is expected to scale as $M^{3/5}$ in agreement with Flory theory (where excluded volume is considered). However, the peptide is a branched polymer that is well structured in a way that the ensemble of linear chains is not. The measured result is a mass scaling that lies between the close-packed scaling and the expectations of the linear chain model. Although the calculation of the diffusion constant of the peptide does not provide a precise measure of the structure of the peptide, it certainly gives an indication that the peptide in solution is not in a completely extended conformation but is rather structured in a more compact way.

End-to-end distance fluctuations

The end-to-end distance in the peptide computed over the four dynamical trajectories is depicted in Fig. 12. The results clearly indicate that the global structure of the peptide is largely intact throughout simulations T1, T2, and T4. This is true in spite of the fact that by a number of measures, including the magnitude of mean-square atomic fluctuations and NMR order parameters, the terminal ends of the peptide are largely disordered. In simulation T3 the behavior is quite different, as there is a strong drift in the end-to-end distance towards shorter distances.

To create a point of reference for our simulation results, it is useful to compare them with a standard of a simple solvable model of an ideal linear polymer. For that model, the end-to-end distribution $W(r_e)$ is a expected to be a Gaussian function

$$W(r_e) = \left(\frac{3}{2\pi\langle r_e^2\rangle}\right)^{3/2} \exp\left[- \frac{3}{2\langle r_e^2\rangle} r_e^2\right] \qquad (15)$$

where $\langle r_e^2\rangle$ is the square of the end-to-end distance averaged over all configurations. For an ideal freely jointed chain, where external forces and hydrodynamic effects are ignored, we expect that $\langle r_e^2\rangle = Nl^2$ where l^2 is the mean-square bond length along the chain and N is the number of bonds. Taking the $C_\alpha - C_\alpha$ distance to be 3.84 Å and $N = 25$ the predicted value is $R_e = \langle r_e^2\rangle^{1/2} = 19.2$ Å. That value sits slightly above the computed values shown in Fig. 12 indicating that the effect of intramolecular interactions and solvation is to reduce the end-to-end distance somewhat relative to the predictions of the freely jointed chain.

Of course, the difference is greater than the deviation of the mean value indicates. This is clearly demonstrated by Fig. 13, which shows the distribution of r_e values computed for the simulated peptide dynamics. In the distribution of r_e the difference is even more pronounced. Unlike a freely jointed chain, the peptide is structured and the range of values of the r_e is severely restricted. The distribution is well approximated by a Gaussian function

$$W(r) \simeq \exp\left(- \frac{(r-\mu)^2}{2\sigma^2}\right) \qquad (16)$$

where μ and σ are the average and the standard deviation, respectively, calculated from the set of data. The parameters of the fits are listed in Table 1.

A point of comparison with experiment is found in the quasielastic light scattering data of Teplow and coworkers (Lomakin, 1997). They measured diffusion constants, which were then interpreted using a Stokes-Einstein analysis (see Eqs. 11 and 12) to derive a distribution of values of the hydrodynamic radius r_H for the peptide. The distribution of radii attributed to the peptide monomer was shown to be spread between 10 and 20 Å. That distribution is in good agreement with the distribution of peptide end-to-end distances derived from our simulations (see Fig. 13).

Radius of gyration

The radius of gyration is a convenient measure of the spatial extent of the peptide during the simulated dynamics. The

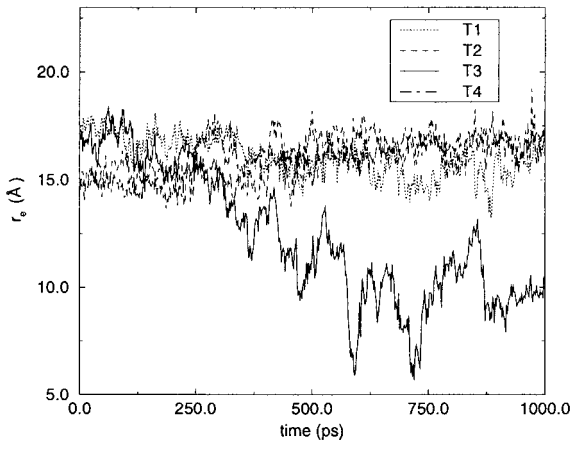

FIGURE 12 The end-to-end distance for the peptide computed for the trajectories T1, T2, T3, and T4.

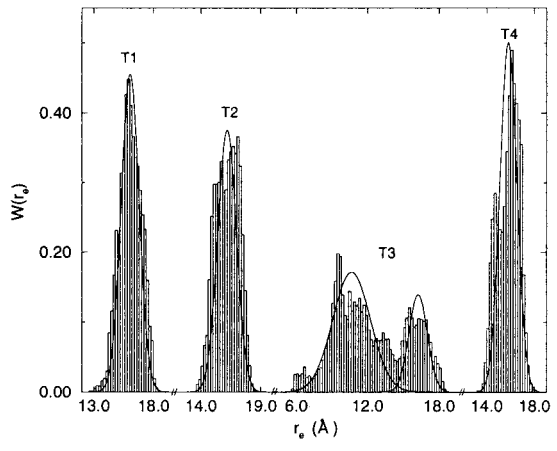

FIGURE 13 The distribution of the instantaneous values of the end-to-end distance of the peptide computed for the trajectories T1, T2, T3, and T4.

TABLE 1 The parameters (in Å) of the Gaussian fits to the distribution of end-to-end distances computed over the four trajectories

	End to end	
Trajectory	μ	σ
1	16.0	0.92
2	16.2	0.96
3 (1st Gaussian)	10.6	1.93
3 (2nd Gaussian)	16.2	0.94
4	15.8	0.87

time dependence of this quantity is depicted in Fig. 14 for the four dynamical simulations. The resulting values provide an estimate of the spatial extent of the molecule that is in good agreement with the estimate of the molecule's hydrodynamic radius.

The time average of the radius of gyration is approximately 9.2 Å, which is in close correspondence with the estimate of the hydrodynamic radius $r_H = 10$ Å computed from the diffusion constant using the Stokes-Einstein relation.

In the simplest approximation of an ideal polymer where excluded volume is ignored, the radius of gyration distribution $W(r_g)$ is a expected to be strongly weighted Gaussian

$$W(r_g) \simeq r_g^6 \exp\left[- \frac{7}{2\langle r_g^2 \rangle} r_g^2 \right]. \quad (17)$$

The radius of gyration was binned over the four simulations and the distributions are plotted in Fig. 15. A fit to the data using the computed values of $\langle r_g^2 \rangle$ is shown for comparison and a Gaussian distribution function (using Eq. 16). This fit approximates the actual distribution satisfactorily over most of its range. The parameters of the fits are listed in Table 2.

We can estimate the radius of gyration from the freely jointed chain model to be

$$\langle r_g^2 \rangle = \frac{1}{6} N \left(\frac{N+2}{N+1} \right) l^2 \quad (18)$$

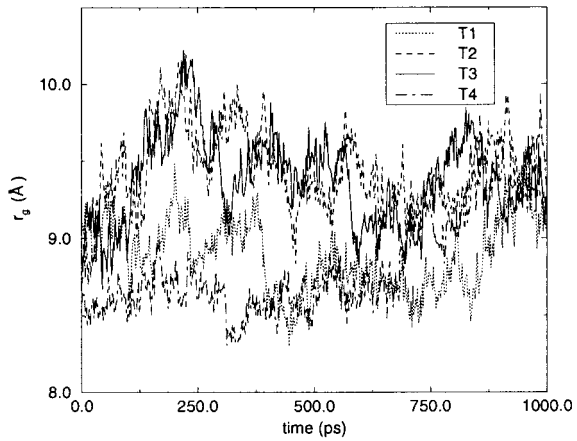

FIGURE 14 The radius of gyration of the peptide computed for the trajectories T1, T2, T3, and T4.

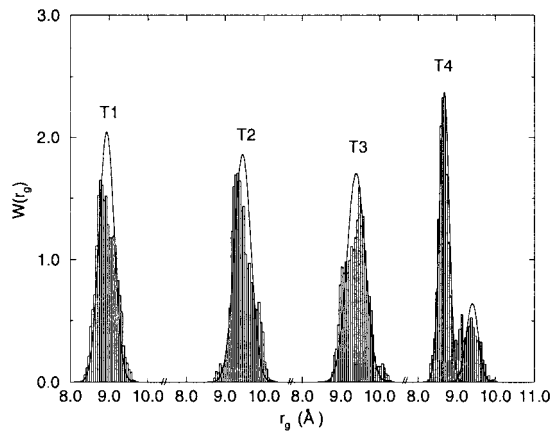

FIGURE 15 The distribution of the instantaneous values of the radius of gyration of the peptide computed for the trajectories T1, T2, T3, and T4.

where N is the number of bonds in the chain and l is the root mean square bond length. In the limit of larger N one finds that $\langle r_g^2 \rangle = \frac{1}{6} \langle r_e^2 \rangle$. For this molecule, we find that on average $\langle r_e^2 \rangle^{1/2} = 16$ Å, so that we would estimate $\langle r_g^2 \rangle^{1/2} = 6.5$ Å, which is somewhat less than our computed value in the range of $\langle r_g^2 \rangle^{1/2} = 10$ Å. This difference results from the fact that the end-to-end distance does not fluctuate widely as is expected in the freely jointed chain model. The peptide has a definite core structure that restricts the range of probable end-to-end distances in the peptide. In this case, that leads to values of $\langle r_e^2 \rangle^{1/2}$ that are smaller than expected.

Characterizing internal motions: Lipari-Szabo NMR order parameters

In Table 3 are listed the computed S^2 order parameters for the four nanosecond simulations of the peptide. The experimentally measured values are listed for comparison. The same data are plotted in Fig. 16 to show better the overall trends across the peptide's primary structure. Comparing the table of S^2 values with the computed RMS fluctuations (see Fig. 7), the correlation is quite good: large values of S^2 correspond with small values of the RMS fluctuation from the average peptide structure.

TABLE 2 The parameters (in Å) of the Gaussian fits to the distribution of radii of gyration computed over the four trajectories

	Radius of gyration	
Trajectory	μ	σ
1	8.93	0.24
2	9.45	0.26
3	9.39	0.29
4 (1st Gaussian)	8.67	0.15
4 (2nd Gaussian)	9.40	0.19

TABLE 3 The computed and experimentally derived values of the S^2 order parameter

	S^2				
Residue	T1	T2	T3	T4	Experimental
Tyr10	0.13	0.16	0.08	0.48	
Glu11	0.44	0.18	0.36	0.51	
Val12	0.67	0.32	0.54	0.69	
His13	0.72	0.24	0.23	0.84	
His14	0.29	0.27	0.42	0.82	
Gln15	0.72	0.54	0.57	0.79	
Lys16	0.81	0.59	0.73	0.85	
Leu17	0.64	0.41	0.79	0.80	
Val18	0.33	0.63	0.80	0.84	0.68 ± 0.05
Phe19	0.58	0.75	0.69	0.85	0.75 ± 0.05
Phe20	0.71	0.69	0.48	0.86	0.79 ± 0.05
Ala21	0.60	0.57	0.10	0.77	
Glu22	0.65	0.65	0.59	0.75	
Asp23	0.54	0.18	0.55	0.78	
Val24	0.68	0.45	0.34	0.74	0.75 ± 0.05
Gly25	0.74	0.61	0.58	0.70	0.76 ± 0.05
Ser26	0.55	0.55	0.33	0.75	
Asn27	0.32	0.55	0.37	0.82	
Lys28	0.69	0.52	0.43	0.82	
Gly29	0.58	0.58	0.34	0.71	0.64 ± 0.06
Ala30	0.38	0.38	0.34	0.68	
Ile31	0.09	0.63	0.28	0.60	
Ile32	0.29	0.75	0.23	0.74	
Gly33	0.26	0.54	0.32	0.60	0.54 ± 0.06
Leu34	0.33	0.22	0.39	0.51	
Met35	0.40	0.25	0.56	0.43	

The residues for which the values of the S^2 order parameter were experimentally measured are shown in bold. Data for key residue Glu22 are underlined.

Simulations T1 and T2 show significant correlations that extend to include the LVFFA and VGS regions. In the T1 simulation, the N terminal end of the peptide shows the higher degree of correlation. In the T2 simulation, it is the C terminal end of the peptide that shows the higher level of correlation.

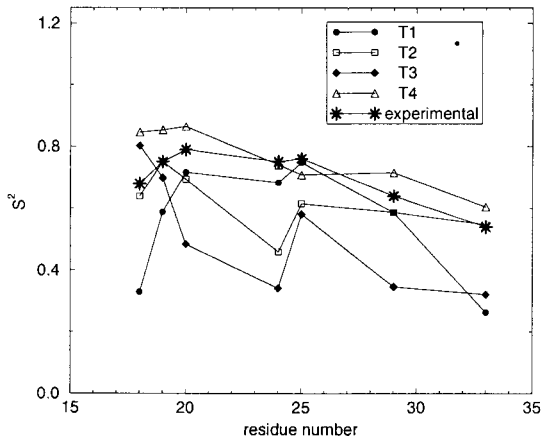

FIGURE 16 Plot of the structural parameter S^2 for the four simulations.

In the T3 run there is significantly less correlation than in the other three trajectories. There are two regions (from Gln15 to Phe19 and Glu22 to Asp23) with larger values of S^2. Note that the FA end of the LVFFA region shows lower values indicating that the LVFFA cluster is disrupted. The structure of the VGSN turn region also appears to be disrupted. It would be interesting to know if that is a consequence of, or reason for, the relatively unstructured nature of the peptide dynamics over that trajectory. In the T3 run, the peptide structure is more open or loose. For example, the Phe19 and Phe20 residues interact with Gly25 and Asp23. Those interactions are not seen in any other trajectory.

In the T3 simulation, Ala21 forms hydrogen bonds not at all or at a very low frequency. This is quite different from all other trajectories in which it is always part of a hydrogen bonding pair. In addition, Leu17 and Val18 do not form any hydrogen bonds with atoms in the region LVFFAEDVGSNK. This could explain the disruption of the core and the fact that $S^2 = 0.1$ for Ala21 in the T3 simulation.

The simulation T4 shows a much higher degree of structure than the other simulations. Values for S^2 exceed 0.5 from Glu11 to Leu34. There are particularly large values in the LVFFA region. This is the simulation that presents the highest number of H-bonds over the entire run. Moreover, the structure of the peptide is significantly more compact in the T4 run than in the other simulations.

Note that the Glu22 shows large S^2 values throughout all four runs. It is the Glu22 residue that is mutated in the E22Q Dutch mutant. This observation is in line with the notion that the WT is less flexible than the E22Q Dutch mutant in the peptide monomer. The greater flexibility in the mutant form may contribute to the faster addition of the peptide monomer to the existing fibril and a larger rate of fibril elongation.

SUMMARY AND CONCLUSIONS

The simulation of four nanosecond trajectories of the wild-type congener amyloid $\beta(10–35)$-NH_2 peptide solvated by 2113 water molecules in a rhombic dodecahedral cell was performed. The analysis of the simulations focused on computing quantities to characterize the structure and dynamics of the peptide. This computational study employed a theoretical model of the peptide in aqueous solution and has provided a number of tests of the model against the results of experiments probing the peptide structure, rate of self-diffusion, conformational fluctuations, and key stabilizing interactions. Particular attention was paid to observables that can be or have been measured experimentally so as to test and validate the theoretical model. The results led to the following conclusions.

1. The computed values of the peptide diffusion constant are consistently on the order of $D = 1.4 \times 10^{-6}\text{cm}^2/\text{s}$ in good agreement with the experimentally measured value of $D_{\text{exp}} = 1.4 \times 10^{-6}\text{cm}^2/\text{s}$ (Tseng et al., 1999). If the simu-

lated peptide structure was significantly different from that of the actual peptide in aqueous solution, the diffusion constants could have been quite different in magnitude. The magnitude of D is consistent with a relatively compact peptide structure.

2. The computed values of the radius of gyration for the peptide, in three of the four simulations, are consistently in the range of $\langle r_g^2 \rangle^{1/2} = 10$ Å. The computed value of the hydrodynamic radius, $r_H = 9.2$ Å is quite similar to this value, indicating that the assumptions underlying the use of the Stokes-Einstein relation are reasonably well satisfied by the dynamics of the Aβ-peptide congener in aqueous solution.

3. Computed NMR order parameters (S^2) are in good agreement with experimentally measured values for three of the four simulations. Evidence suggests that the LVFFA cluster and VGSN turn are cooperatively stabilized through intramotif hydrogen bonds.

4. Simulations suggest that the LVFFA hydrophobic cluster and VGSN turn are particularly stable in agreement with chemical shift data. The general trends in the magnitude of the root-mean-square atomic fluctuations compare well with the trends in the magnitude of the chemical shift data.

All of these results suggest that the theoretical model employed provides an accurate representation of the peptide structure and dynamics in solution.

An understanding of the mechanism of in vivo amyloid fibril formation and elongation is an important goal that is best reached by a combination of experimental and computational studies. Our simulation study indicates that the peptide is somewhat disordered in solution. As a result, characterization of the peptide structure and dynamics is difficult using NMR probes alone. The solution structure of the monomeric peptide is central to the understanding of peptide-peptide association and aggregation to form amyloid fibrils. To unravel the mechanism of amyloid fibril formation, it will be necessary to understand the solution structure and dynamics of the monomeric peptide in solution.

Future directions in the simulation of the Aβ peptide should consist of the simulation of mutant forms of the peptide that show strongly differing rates of fibril elongation. The details of peptide-peptide interactions must be explored to recognize the importance of monomeric peptide conformational transitions in peptide aggregation and protofibril formation.

J. E. S. gratefully acknowledges the National Science Foundation for support and the Center for Computational Science at Boston University for essential computational resources. J. P. L. acknowedges the support of the National Institutes of Health (NIH R29 AG13735).

REFERENCES

Barrow, C. J., A. Yasuda, P. T. Kenny, and M. G. Zagorksi. 1992. Solution conformations and aggregational properties of synthetic amyloid β-peptides of Alzheimer's-disease: analysis of circular-dichroism spectra. *J. Mol. Biol.* 225:1075–1093.

Berne, B. J., and R. Pecora. 1976. Dynamic Light Scattering. Wiley-Interscience, New York, NY.

Brooks, B., R. Bruccoleri, B. Olafson, D. States, S. Swaninathan, and M. Karplus. 1983. Charmm: a program for macromolecular energy minimization and dynamics calculations. *J. Comp. Chem.* 4:187–217.

Cavanagh, J., W. J. Fairbrother, A. G. P. III, and N. J. Skelton. 1996. Protein nmr spectroscopy: Principles and practice. Academic Press, Inc., San Diego, CA.

Esler, W. P., A. M. Felix, E. R. Stimson, J. R. Ghiraldi, Y.-A. Lu, H. V. Vinters, P. W. Mantyh, J. P. Lee, and J. E. Maggio. 2000. Activation barriers to structural transition determine deposition rates of Alzheimer's disease Aβ amyloid. *J. Struct. Biol.* 130:174–183.

Esler, W. P., E. R. Stimson, J. R. Ghilardi, H. V. Vinters, J. P. Lee, P. W. Mantyh, and J. E. Maggio. 1996a. In vitro growth of Alzheimer's disease beta-amyloid plaques displays first-order kinetics. *Biochemistry.* 35: 749–757.

Esler, W. P., E. R. Stimson, J. R. Ghilardi, Y. A. Yu, A. M. Felix, H. V. Vinters, P. W. M. J. P. Lee, and J. E. Maggio. 1996b. Point substitution in the central hydrophobic cluster of a human β-amyloid congener disrupts peptide folding and abolishes plaque competence. *Biochemistry.* 35:13914–13921.

Harper, J. D., S. S. Wong, C. M. Lieber, and J. P. T. Lansbury. 1997a. Observation of metastable Aβ amyloid protofibrils by atomic force microscopy. *Chem. Biol.* 4:119–125.

Harper, J. D., S. S. Wong, C. M. Lieber, and J. P. T. Lansbury. 1997b. Atomic force microscopic imaging of seeded fibril formation and fibril branching by the Alzheimer's disease amyloid-β protein. *Chem. Biol.* 4:951–959.

Kusumoto, Y., A. Lomakin, D. B. Teplow, and G. B. Bendek. 1998. Temperature dependence of amyloid β-protein fibrillization. *Proc. Natl. Acad. Sci. USA.* 95:12277–12282.

Lansbury, P. T. Jr. 1996. A reductionist view of Alzheimer's disease. *Acc. Chem. Res.,* 29:317–321.

Lee, B., and F. M. Richards. 1971. Interpretation of protein structures: Estimation of static accessibility. *J. Mol. Biol.* 55:379–400.

Lee, J. P., E. R. Stimson, J. R. Ghilardi, P. W. Mantyh, Y.-A. Lu, A. M. Felix, W. Llanos, A. Behbin, M. Cummings, M. V. Criekinge, W. Timms, and J. E. Maggio. 1995. ^{1}H NMR of Aβ amyloid peptide congeners in water solution. Conformational changes correlate with plaque competence. *Biochemistry,* 34:5191–5200.

Lipari, G., and A. Szabo. 1982a. Model free approach to the interpretation of nuclear magnetic resonance relaxation in macromolecules: 1. Theory and range of validity. *J. Am. Chem. Soc.* 104:4546–4559.

Lipari, G., and A. Szabo. 1982b. Model free approach to the interpretation of Nuclear Magnetic Resonance relaxation in macromolecules: 1. Analysis of experimental results, *J. Am. Chem. Soc.* 104:4559–4570.

Lomakin, A., D. S. Chung, G. B. Benedek, D. A. Kirscher, and D. B. Teplow. 1996. On the nucleation and growth of amyloid β-protein fibrils: Detection of nuclei and quantitation of rate constants. *Proc. Natl. Acad. Sci. USA.* 93:1125–1129.

Lomakin, A., D. B. Teplow, D. A. Kirschner, and G. B. Bendek. 1997. Kinetic theory of fibrillogenesis of amyloid β-protein. *Proc. Natl. Acad. Sci. USA.* 94:7942–7947.

Mackerell, Jr., A. D., D. Bashford, M. Bellott, R. L. D. Jr., J. D. Evanseck, M. J. Field, S. Fischer, J. Gao, H. Guo, S. Ha, D. Joseph-McCarthy, L. Kuchnir, K. Kuczera, F. T. K. Lau, C. Mattos, S. Michnick, T. Ngo, D. T. Nguyen, B. Prodhom, I. W. E. Reiher, B. Roux, M. Schlenkricha, J. C. Smith, R. Stote, J. E. Straub, M. Watanabe, J. Wiokiewicz-Kuczera, D. Yin, and M. Karplus. 1998. All-atom empirical potential for molecular modeling and dynamics studies of proteins. *J. Phys. Chem. B.* 102:3586–3616.

Maggio, J. E. and P. W. Mantyh. 1996. Brain amyloid: a physicochemical perspective. *Brain Pathol.* 6:147–162.

Peng, J. W. and G. Wagner. 1992. Mapping of the spectral densities of the N-H bond motions in eglin c using heteronuclear relaxation experiments. *Biochemistry.* 31:8571–8586.

Peng, J. W., and G. Wagner. 1995. Frequency spectrum of NH bonds in eglin c from spectral density mapping at multiple fields. *Biochemistry.* 34:16733–16752.

Philippopoulos, M., and C. Lim. 1994. Internal motions in the molecular tumbling regime: effect on NMR dipolar cross relaxation and interproton distance determination. *J. Phys. Chem.* 98:8264–8273.

Rochet, J.-C., and J. P. T. Lansbury. 2000. Amyloid fibrillogenesis: themes and variations. *Curr. Opin. Struc. Biol.* 10:60–68.

Selkoe, D. J. 1991. Alzheimer's disease: a central role for amyloid. *J. Neuropath. Exp. Neurol.* 53:438–447.

Simmerling, C., R. Elber, and J. Zhang. 1995. A program for visualization of structure and dynamics of biomolecules and STO: a program for computing stochastic paths. *In* Modelling of Biomolecular Structure and Mechanisms. A. Pullman, J. Jortner, B. Pulman, eds. Kluwer, Dordrecht, The Netherlands. 241–265.

Teplow, D. B. 1998. Structural and kinetic features of amyloid β-protein fibrillogenesis. *Amyloid: Int. J. Exp. Clin. Invest.* 5:121–142.

Tseng, B. P., W. P. Esler, C. B. Clish, E. R. Stimson, J. R. Ghilardi, H. V. Vinters, P. W. Mantyh, J. P. Lee, and J. E. Maggio. 1999. Deposition of monomeric, not oligomeric, Aβ mediates growth of Alzheimer's disease amyloid plaques in human brain preparations. *Biochemistry.* 38: 10424–10431.

Walsh, D. M., A. Lomakin, G. B. Bendek, M. M. Condron, and D. B. Teplow. 1997. Amyloid β-protein fibrillogenesis: Detection of a protofibrillar intermediate. *J. Biol. Chem.,* 272:22364–22372.

Wesson, L., and D. Eisenberg. 1992. Atomic solvation parameters applied to molecular dynamics of proteins in solution. *Protein Sci.,* 1:227–235.

Zhang, S. 1999. Studies of β amyloid congeners directed toward understanding the molecular mechanism underlying the formation of amyloid deposits in Alzheimer's disease. Ph.D. Thesis, Boston University, Boston, MA. 187 pp.

Zhang, S., K. Iwata, M. J. Lachenman, J. W. Peng, S. Li, E. R. Stimson, Y. A. Lu, A. M. Felix, J. E. Maggio, and J. P. Lee. 2000. The Alzheimer's peptide Aβ adopts a collapsed coil structure in water. *J. Struct. Biol.* 130:130–141

Zhang, S. S., N. Casey, and J. P. Lee. 1998. Residual structure in the Alzheimer's disease peptide: probing the origin of a central hydrophobic cluster. *Fold. Des.* 3:413–422.